

# Gravitational wave detection of DFSZ axion models

Aidi Yang<sup>1,\*</sup> and Fa Peng Huang<sup>1,†</sup>

<sup>1</sup>*MOE Key Laboratory of TianQin Mission,  
TianQin Research Center for Gravitational Physics & School of Physics and Astronomy,  
Frontiers Science Center for TianQin,  
Gravitational Wave Research Center of CNSA,  
Sun Yat-sen University (Zhuhai Campus), Zhuhai 519082, China*

## Abstract

As a promising dark matter candidate, the axion particle can naturally solve the strong CP problem of the standard model through the U(1) Peccei-Quinn symmetry-breaking process. However, detecting this high-energy process poses a significant challenge for colliders. We precisely calculate the phase transition gravitational wave signals of this symmetry-breaking process in the popular DFSZ axion model. By comparing the signals with the expected sensitivity of Cosmic Explorer and Einstein Telescope, we demonstrate that Cosmic Explorer could detect this process with a signal-to-noise ratio higher than 8 for the benchmark points. Furthermore, by performing Fisher analysis, we find that if signals are observed, the bubble wall velocity will be the first phase transition parameter to be determined. The future gravitational wave detectors are expected to provide a new approach to exploring concrete axion models.

---

\* yangai@mail2.sysu.edu.cn

† huangfp8@sysu.edu.cn

## I. INTRODUCTION

The strong CP problem in the standard model and the microscopic nature of dark matter are long-standing fundamental problems in particle physics and cosmology. Axion particle [1–9] can naturally solve the strong CP problem and also be a promising dark matter candidate simply through the misalignment mechanism [10–12]. The U(1) Peccei-Quinn (PQ) symmetry-breaking process is essential to solve the strong CP problem [1, 2]. The scale of the PQ symmetry breaking process determines the axion mass and its couplings with the standard model particles. Thus, it is important to explore the PQ symmetry breaking scale and the symmetry breaking dynamics by experiments. However, the colliders and other traditional experiments are challenging to detect this high-energy process. Motivated by the great achievements of gravitational wave (GW) observations, we consider the possible GW detection of the dynamical process of the U(1) PQ symmetry breaking since in the early universe the PQ symmetry breaking process might generate a strong first-order phase transition(SFOPT) [13–17]. In this case, an observable stochastic gravitational wave background (SGWB) can be produced. We investigate the possibility of exploring this symmetry-breaking process through GW experiments. Taking one concrete model of Dine-Fischler-Srednicki-Zhitnitsky (DFSZ) axion theory as a typical example [7, 8], we precisely calculate the phase transition dynamics and its associated phase transition GW signals from bubble collisions [18–22], sound waves [23, 24], and turbulence [25, 26]. Compared with the expected sensitivity curves of Cosmic Explorer (CE) [27–30] and the Einstein Telescope (ET) [31, 32]. We demonstrate that the GW signals from axion models can be detected by CE with a signal-to-noise ratio (SNR) higher than 8. Furthermore, using the method of Fisher matrix (FM) [33], we find that the bubble wall velocity will be the first phase transition parameter to be fixed if the signals are observed.

For the sake of integrity, we briefly review the axion models in Sec. II and the detection principles of SGWB in Sec. III. Readers familiar with these two sections can skip them and proceed directly to Sec. IV. In Sec. IV, we precisely calculate the phase transition GW signals generated by the PQ symmetry breaking process in the DFSZ model and discuss their detectability at future GW detectors, such as CE and ET. Then, we perform Fisher analysis for the key phase transition parameters at CE in Sec. V. A summary is given in Sec. VI. More details are shown in the Appendix.

## II. AXION AND DFSZ MODELS

### A. Strong CP problem and axion solution

As a  $SU(3)_c$  non-Abelian gauge theory in 4-dimensional spacetime, the QCD Lagrangian density contains a CP violation term originating from the instanton effects

$$\mathcal{L}_{\text{QCD}} \supset \bar{\theta} \frac{g_s^2}{32\pi^2} G^{a\mu\nu} \tilde{G}_{a\mu\nu} \quad (1)$$

where  $g_s$  is the  $SU(3)_c$  gauge coupling constant,  $G^{a\mu\nu}$  is the gluon field-strength tensor, and  $\tilde{G}_{a\mu\nu}$  is the dual of the gluon field-strength tensor. This CP-violating  $\bar{\theta}$  can induce a neutron electric dipole moment of order [34]

$$d_n^{(th)} \simeq 2.4(1.0) \times 10^{-16} \bar{\theta} \text{ e cm} \quad (2)$$

However, current experiments give an upper bound to the electric dipole moment of the neutron as [35, 36]

$$|d_n^{(exp)}| < 1.8 \times 10^{-26} \text{ e cm} \quad (3)$$

This requires negligible  $\bar{\theta}$ , namely,

$$\bar{\theta} < 10^{-10} \quad (4)$$

Why is the  $\bar{\theta}$  parameter in QCD so small? This is the so-called strong CP problem in the standard model of particle physics.

Axion models provide natural solutions to dynamically explain the strong CP problem. The strong CP problem can be resolved by introducing a new global U(1) PQ symmetry. When the U(1) PQ symmetry is spontaneously broken, it gives rise to a new Nambu-Goldstone boson called axion. The mass and interaction properties of the axion are closely related to the introduced PQ scalar field  $\sigma$ . The interaction between the axion field  $a$  and the gluon field takes the form of  $aG\tilde{G}/f_a$ , where  $f_a$  is the decay constant of the axion. The presence of the axion allows for the replacement of the CP-violating term  $\bar{\theta}$  with a dynamic field known as the axion field. The axion field dynamically adjusts itself to a value that effectively cancels out the  $\bar{\theta}$  by sitting at the minimum of the axion potential. Within this dynamical mechanism, the strong CP problem is solved by the emergence of the axion particle.

The original Peccei-Quinn-Weinberg-Wilczek (PQWW) axion model [1–4] assumed the PQ symmetry breaking happens just at the electroweak energy scale, namely,

$$f_a \simeq 246 \text{ GeV}. \quad (5)$$

It was immediately excluded by experimental data, including beam-dump and LEP experiments results [37, 38]. Later, two types of invisible axion models are proposed with much higher PQ energy scale to decrease the axion mass and reduce its couplings to ordinary matter,

$$f_a \gg 246 \text{ GeV} \quad (6)$$

## B. Invisible axion model

### 1. Kim-Shifman-Vainshtein-Zakharov model

One type of invisible axion is the Kim-Shifman-Vainshtein-Zakharov (KSVZ) model where exotic quark  $Q_E + Q_E^C$  with the and a new complex gauge-singlet scalar  $\sigma$  are included [5, 6, 39]. The relevant Lagrangian density is

$$\mathcal{L}_{\text{KSVZ}} \supset \lambda_K \sigma Q_E Q_E^C - \lambda \left( |\sigma|^2 - \frac{f_a^2}{2} \right)^2 \quad (7)$$

All standard model fields are neutral under the  $U(1)$  PQ symmetry in its linear realization. The PQ charge of the scalar field  $X_\sigma = 1$  and the PQ charge of the exotic quark  $X_{Q_E} = X_{Q_E^C} = -1/2$ . The Yukawa coupling constant  $\lambda_K$  plays a crucial role in this model and can be treated as a free parameter. This term facilitates the interaction between the PQ field and the heavy exotic quarks. Like the PQWW model, a global  $U(1)$  PQ symmetry generates a shift in the axion field through a chiral rotation. However, the potential in this model spontaneously breaks the global  $U(1)$  PQ symmetry. Therefore, the KSVZ model offers a solution to the strong CP problem.

### 2. Dine-Fischler-Srednicki-Zhitnitsky model

In this work, we focus on the other type of invisible axion model, namely, the well-known DFSZ model. All the standard model fields are PQ-charged as the original PQWW model. This model consists of two Higgs doublets and a complex scalar field, denoted as  $\sigma$ . As

one component of the complex scalar field, the DFSZ axion is linked to the standard model through the two Higgs doublets  $H_u$  and  $H_d$ . The scalar field transforms according to the following expression

$$\sigma \rightarrow e^{iX_\sigma\gamma}\sigma, \quad H_u \rightarrow e^{iX_u\gamma}H_u, \quad H_d \rightarrow e^{iX_d\gamma}H_d \quad (8)$$

where

$$X_u + X_d = 2X_\sigma = 1 \quad (9)$$

The general tree-level potential is [8]

$$\begin{aligned} V(\sigma, H_u, H_d) = & \lambda_u (|H_u|^2 - v_u^2)^2 + \lambda_d (|H_d|^2 - v_d^2)^2 \\ & + \lambda (|\sigma|^2 - v_\sigma^2)^2 + (\lambda_a |H_u|^2 + \lambda_b |H_d|^2) |\sigma|^2 \\ & + \lambda_c (H_u^i \epsilon_{ij} H_d^j \sigma^n + \text{h.c.}) + \lambda_d |H_u^i \epsilon_{ij} H_d^j|^2 + \lambda_e |H_u^* H_d|^2 \end{aligned} \quad (10)$$

where  $n = 1/X_\sigma$  ( $X_\sigma$  is PQ charge of  $\sigma$ ),  $v_\sigma$  is the vev of the  $\sigma$ . Additionally, all couplings in this model are assumed to be real. The proposed model suggests that  $n$  is equal to 2, and the number parameter of the domain wall is denoted by  $N_{DW}$ , which is 6. We set  $X_u = 1$ ,  $X_d = 0$ , and  $X_\sigma = \frac{1}{2}$ . As before, the potential spontaneously breaks the global U(1) PQ symmetry. Our research focused on calculating the first DFSZ-type models, specifically the minimal DFSZ model known as DFSZ-I. In DFSZ-I, only an additional complex scalar field with  $n = 2$  is introduced.

### C. axion dark matter and axion detection

Axion particles can be a natural dark matter candidate produced by the misalignment mechanism. There are various experiments to detect the axion particles or axion dark matter, such as helioscope searches [40–42], haloscopes [43], and the radio telescope searches [44–46], see recent review [9] for details. GW might provide new approaches to explore axion [13–17, 47–51]. To explore the possibility that the DFSZ axion model can generate an observable SGWB, we continue to review the detection principles of the SGWB and the sensitivity curves of GW detectors in the next section. This will lay the foundation for us to calculate the strength of the phase transition GW signals predicted by the DFSZ model and evaluate their detectability in Sec.IV.

### III. STOCHASTIC GRAVITATIONAL WAVE BACKGROUND DETECTION

The theoretical framework of the DFSZ axion model in the last section predicts that it might generate a SFOPT, which in turn can produce an observable SGWB. Unlike GW signals from individual astrophysical events, SGWB [52–54] arises from the superposition of GWs emitted by countless sources across the universe, such as binary mergers, supernova explosions, cosmic strings, and other astrophysical processes. As the SGWB originates from all directions and consists of GWs with different frequencies, its signal is typically weak and distributed over a wide frequency range. We cannot directly measure the properties of individual SGWB sources. To detect the SGWB, multiple GW detectors are typically employed to observe simultaneously, and their data is subjected to long-term integration and cross-correlation analysis. The correlation analysis of the GW detector network can extract the SGWB signal. In this section, we briefly summarize the key points for SGWB detection [55].

#### A. Signal analysis

In the actual detection process, the output signal of the detector  $s_{gw}(t)$  consists of the GW signal  $h_{gw}(t)$  and noise  $n_{gw}(t)$

$$s_{gw}(t) = h_{gw}(t) + n_{gw}(t) \quad (11)$$

Here, it is assumed that the noise  $n_{gw}(t)$  is a stationary random process, and its autocorrelation function depends only on the time difference, not on the specific time point. The autocorrelation function of the noise  $R(\tau)$  is defined as

$$R(\tau) = \langle n_{gw}(t)n_{gw}(t + \tau) \rangle = \int_{-\infty}^{\infty} n_{gw}(t)n_{gw}(t + \tau)dt \quad (12)$$

The noise power spectral density (PSD) function  $S_n(f)$  describes the distribution of noise power in the frequency domain. According to the Wiener-Khinchin theorem, there exists a Fourier transform relationship between the autocorrelation function and the PSD for a stationary random process. For a stationary random process,  $\langle \tilde{n}_{gw}^*(f)\tilde{n}_{gw}(f') \rangle$  is non-zero only when  $f = f'$  ( $\tilde{n}_{gw}(f)$  is Fourier transform of  $n_{gw}(t)$ ). Combining these concepts, we obtain the following equation

$$\langle \tilde{n}_{gw}^*(f)\tilde{n}_{gw}(f') \rangle = \delta(f - f') \frac{1}{2} S_n(f) \quad (13)$$

Eq. (13) describes the statistical properties of stationary random noise in the frequency domain. Since  $n_{gw}(t)$  is real,  $\tilde{n}_{gw}(-f) = \tilde{n}_{gw}^*(f)$  and  $S_n(-f) = S_n(f)$ . Limiting the time interval to  $-T_t/2 < t < T_t/2$ ,  $T_t$  is the observation time. We have

$$\delta(f=0) \rightarrow \left[ \int_{-T_t/2}^{T_t/2} dt e^{i2\pi ft} \right]_{f=0} = T_t \quad (14)$$

Therefore, it can be derived that  $n_{gw}^2(t) = \int_0^\infty df S_n(f)$ . This formula shows how  $S_n(f)$  is associated with the mean square value of the noise in the time domain. Other methods are usually used to analyze the noise signal, such as using the PSD or autocorrelation function of the noise. The general form of the detector output is given by Eq. (11). To extract the GW signal from the noise, the cross-correlation between the GW signal and the detector signal is calculated first

$$\frac{1}{T_t} \int_0^{T_t} dt s_{gw}(t) h_{gw}(t) = \frac{1}{T_t} \int_0^{T_t} h_{gw}^2(t) + \frac{1}{T_t} \int_0^{T_t} dt n_{gw}(t) h_{gw}(t) \quad (15)$$

then

$$\frac{1}{T_t} \int_0^{T_t} dt h_{gw}^2(t) \sim h_0^2 \quad (16)$$

where  $h_0$  is the characteristic amplitude of  $h_{gw}(t)$ . Since the noise  $n_{gw}(t)$  and the signal  $h_{gw}(t)$  are uncorrelated [55]

$$\frac{1}{T_t} \int_0^{T_t} dt n_{gw}(t) h_{gw}(t) \sim \left( \frac{T_0}{T_t} \right)^{1/2} n_0 h_0 \quad (17)$$

where  $n_0$  is the characteristic amplitude of  $n_{gw}(t)$ .  $T_0$  is the oscillation period. Assuming we know the form of  $h_{gw}(t)$ , then we consider which filter function can maximize the SNR. This technique is called matched filtering.

$$\hat{s} = \int_{-\infty}^{\infty} dt s_{gw}(t) K(t) \quad (18)$$

where  $K(t)$  is called the filter function. SNR is defined as  $S/N$  with  $S$  being the expected value of  $\hat{s}$  when the signal is present, and  $N$  is the root mean square value of  $\hat{s}$  when the signal is absent. Because  $\langle n_{gw}(t) \rangle = 0$ , we have

$$\begin{aligned} S &= \int_{-\infty}^{\infty} dt \langle s_{gw}(t) \rangle K(t) \\ &= \int_{-\infty}^{\infty} dt h_{gw}(t) K(t) \\ &= \int_{-\infty}^{\infty} df \tilde{h}_{gw}(f) \tilde{K}^*(f) \end{aligned} \quad (19)$$

In the absence of a signal, the variance of  $N^2$  can be obtained by calculating the convolution of  $K(t)$  with  $R(\tau)$  which is given by Eq. (12)

$$\begin{aligned} N^2 &= \int_{-\infty}^{\infty} dt dt' K(t) K(t') \int_{-\infty}^{\infty} df \frac{1}{2} S_n(f) e^{2\pi i f(t-t')} \\ &= \int_{-\infty}^{\infty} df \frac{1}{2} S_n(f) |\tilde{K}(f)|^2 \end{aligned} \quad (20)$$

Therefore, the SNR for a single detector is

$$SNR_{\text{single}} = \frac{\int_{-\infty}^{\infty} df \tilde{h}_{gw}(f) \tilde{K}^*(f)}{\left[ \int_{-\infty}^{\infty} df \frac{1}{2} S_n(f) |\tilde{K}(f)|^2 \right]^{1/2}} \quad (21)$$

A single detector cannot effectively distinguish between SGWB signals and detector noise because they both have random properties. However, by using two detectors and comparing their outputs, the SGWB signal can be extracted [54]. This is achieved by calculating the cross-correlation function between the outputs of the two detectors. To optimize the SNR, a filter function  $Q(t)$  is introduced [55]. The differences in the locations and orientations of the two detectors affect the correlation of the GW signals they detect, which can be described by the overlap reduction function  $\Gamma(f)$  [54]. To maximize the SNR ratio, the filter function  $\tilde{Q}(f)$  which is the Fourier transform of  $Q(t)$ , needs to be optimized. The optimized expression for the SNR is

$$SNR_{\text{optimized}} = T_t^{1/2} \frac{\int_{-\infty}^{\infty} df S_h(f) \Gamma(f) \tilde{Q}(f)}{\left[ \int_{-\infty}^{\infty} df |\tilde{Q}(f)|^2 S_{2n}^2(f) \right]^{1/2}} \quad (22)$$

where  $S_h(f)$  is the PSD of the SGWB, and  $S_{2n}(f) = [S_{n,1}(f) S_{n,2}(f)]^{1/2}$  is the geometric mean of the noise spectral densities of the two detectors. The goal is to find the optimal form of  $\tilde{Q}(f)$  that maximizes the SNR expression. This optimization problem can be solved using the Schwarz inequality, which states that for any two functions  $u(f)$  and  $v(f)$

$$\left| \int_{-\infty}^{\infty} df u(f) v^*(f) \right|^2 \leq \int_{-\infty}^{\infty} df |u(f)|^2 \int_{-\infty}^{\infty} df |v(f)|^2 \quad (23)$$

with equality holding if and only if  $u(f) = \lambda_s v(f)$  for some constant  $\lambda_s$ . We can identify

$$u(f) = S_h(f) \Gamma(f) \tilde{Q}(f), \quad v(f) = \frac{1}{S_{2n}(f)} \quad (24)$$

Applying the Schwarz inequality, we obtain

$$SNR_{\text{optimized}} \leq T_t^{1/2} \left[ \int_{-\infty}^{\infty} df \frac{S_h^2(f) \Gamma^2(f)}{S_{2n}^2(f)} \right]^{1/2} \quad (25)$$

with equality holding if and only if

$$\tilde{Q}(f) = \lambda_s \frac{S_h(f)\Gamma(f)}{S_{2n}^2(f)} \quad (26)$$

This result gives the optimal form of the filter function  $\tilde{Q}(f)$  that maximizes the SNR. To quantify the detectability of the GW signal in a given model with SFOPT, the SNR needs to be calculated

$$SNR_{\text{gw}} = \sqrt{T_t \int_{f_{\min}}^{f_{\max}} df \left( \frac{h_{100}^2 \Omega_{\text{GW}}}{h_{100}^2 \Omega_{\text{sens}}} \right)^2} \quad (27)$$

where  $h_{100} = 0.72$  eliminates sensitivity to the observed value of the Hubble constant  $H_0$

$$H_0 = h_{100} \times 100 \text{ km s}^{-1} \text{Mpc}^{-1} \quad (28)$$

$h_{100}^2 \Omega_{\text{sens}}$  corresponds to the expected sensitivity for given detectors. To demonstrate the detectability of GW signals, we calculate their SNR and compare it with the threshold SNR value of the detector. If the calculated SNR is larger than the threshold, the detector can detect the GW signal. To better understand the sensitivity of a detector, we need to consider the sensitivity curve.

## B. Sensitivity curves

The sensitivity curve of a detector characterizes its ability to detect signals. The three commonly used definitions for sensitivity curves are the characteristic strain, the amplitude spectral density, and the energy density [56].

### 1. The characteristic strain

The characteristic strain denoted as  $h_c(f)$  can be derived from the metric perturbations (GW)  $h_{ab}(t, \vec{x})$

$$h_{ab}(t, \vec{x}) = \sum_A \int_{-\infty}^{\infty} df \int_{S^2} d\hat{\Omega} h_A(f, \hat{\Omega}) e^{i2\pi f(t - \hat{\Omega} \cdot \vec{x})} e_{ab}^A(\hat{\Omega}) \quad (29)$$

where  $h_A(f, \hat{k})$  is the Fourier transformation of  $h_{ab}(t, \vec{x})$ .  $e_{ab}^A(\hat{k})$  represents the polarization tensors for GWs, with  $A$  taking values of  $+$  and  $\times$ . Additionally, we introduce  $\hat{\Omega}$  as a unit

vector denoting a specific direction on the two-sphere and  $\hat{k} = 2\pi f \hat{\Omega}$ . The characteristic strain  $h_c(f)$  for GWs is defined as

$$\left\langle h_A(f, \hat{k}) h_{A'}^*(f', \hat{k}') \right\rangle = \frac{1}{16\pi} \delta(f - f') \delta_{AA'} \delta^2(\hat{k}, \hat{k}') h_c(f)^2 f^{-1} \quad (30)$$

where  $\delta_{AA'}$  indicates that GWs with different polarization states are uncorrelated.  $\delta^2(\hat{k}, \hat{k}')$  is the delta function on the sphere which indicates that GWs propagating in different directions are uncorrelated. The characteristic strain noise amplitude for a single detector is denoted by  $h_n(f)$ .

### 2. The strain power spectral density

The strain PSD of a GW,  $S_h(f)$ , is known to have a relationship with  $h_c(f)$  [56]

$$\sqrt{S_h(f)} = h_c(f) f^{-1/2} \quad (31)$$

By comparison, an equivalent expression for the strain noise PSD  $S_n(f)$  can be established

$$\sqrt{S_n(f)} = h_n(f) f^{-1/2} \quad (32)$$

### 3. The energy density $\Omega_{\text{gw}}(f)$

In cosmology, one usually use the variable  $\Omega_{\text{gw}}(f)$  which signifies the fractional contribution of the GW energy density [54]

$$\Omega_{\text{gw}}(f) = \frac{1}{\rho_c} \frac{d\rho_{\text{gw}}}{d \ln f} \quad (33)$$

where  $\rho_c$  is the critical energy density. We have the following conversion formula

$$\Omega_{\text{gw}}(f) = \frac{2\pi^2}{3H_0^2} f^2 h_c^2(f) = \frac{2\pi^2 S_h(f)}{3H_0^2} f^3 \quad (34)$$

The quantity frequently depicted on sensitivity curves for energy density is the  $\Omega_{\text{gw}}(f) h_{100}^2$ .

## IV. PHASE TRANSITION GRAVITATIONAL WAVE OF THE DFSZ-I AXION MODEL AND ITS SNR AT COSMIC EXPLORER

In the previous section, we reviewed the detection principles of the SGWB and introduced the sensitivity curves of GW detectors. This lays the foundation for our discussion on the

SFOPT signals generated by the DFSZ-I axion model in this section. We will calculate in detail the SFOPT signals produced in the DFSZ-I model and evaluate their SNR and detectability at the future GW detectors CE and ET. In this section, we use the finite-temperature effective field theory [57, 58] to investigate the phase transition dynamics in DFSZ-I. At zero temperature, the tree-level potential is given by [8]

$$\begin{aligned}
V_{\text{tree}} = & -\mu_1^2 |H_u|^2 - \mu_2^2 |H_d|^2 + \lambda_1 |H_u|^4 + \lambda_2 |H_d|^4 + \lambda_4 |H_u^\dagger H_d|^2 \\
& - \mu_3^2 |\sigma|^2 + \lambda_3 |\sigma|^4 + \lambda_{12} |H_u|^2 |H_d|^2 + \lambda_{13} |\sigma|^2 |H_u|^2 \\
& + \lambda_{23} |\sigma|^2 |H_d|^2 + \left( \lambda_5 \sigma^2 \tilde{H}_u^\dagger H_d + \text{h.c.} \right)
\end{aligned} \tag{35}$$

where the doublet  $\tilde{H}_u = i\tau_2 H_u^*$  and  $\sigma$  is a complex singlet. At the scale of PQ symmetry breaking, only the  $\sigma$  field acquires a vacuum expectation value (vev). The vev of the  $\sigma$  field is denoted as  $\langle \sigma \rangle = \frac{v_\sigma}{\sqrt{2}}$ . The singlet and doublets can be expanded as follows

$$\sigma = \frac{1}{\sqrt{2}} (v_\sigma + \sigma^0 + i\eta_\sigma^0) \tag{36}$$

$$H_u = \begin{pmatrix} h_u^R + ih_u^I \\ \frac{1}{\sqrt{2}}(h_u^0 + i\eta_u^0) \end{pmatrix} \tag{37}$$

$$H_d = \begin{pmatrix} \frac{1}{\sqrt{2}}(h_d^0 + i\eta_d^0) \\ h_d^R + ih_d^I \end{pmatrix} \tag{38}$$

The free energy density of the scalar field is the effective potential. Generally, the effective potential is composed of three parts

$$V_{\text{eff}}(v_\sigma, T) \equiv V_{\text{tree}}(v_\sigma) + V_{\text{CW}}(v_\sigma) + V_{\text{T}}(v_\sigma, T) \tag{39}$$

where  $T$  is temperature and  $V_{\text{tree}}$  refers to the tree-level potential.  $V_{\text{CW}}(v_\sigma)$  denotes the one-loop corrections at the zero temperature.  $V_{\text{T}}(v_\sigma, T)$  represents the thermal correction including the daisy resummation at finite temperature. The tree-level potential can be simplified as

$$V_{\text{tree}}(v_\sigma) = -\frac{1}{2}\mu_3^2 v_\sigma^2 + \frac{1}{4}\lambda_3 v_\sigma^4 \tag{40}$$

In the  $\overline{MS}$  scheme [57], the zero-temperature Coleman-Weinberg (CW) potential can be expressed as follows

$$V_{\text{CW}}(v_\sigma) = \frac{1}{64\pi^2} \sum_S n_S m_S^4(v_\sigma) \left[ \log \frac{m_S^2(v_\sigma)}{\mu^2} - \frac{3}{2} \right] \tag{41}$$

where  $m_S(v_\sigma)$  represents the field-dependent mass and  $n_S$  is the degree of freedom (*d.o.f.*).  $\mu$  represents the renormalization scale, and the constant  $\frac{3}{2}$  is for scalars. The thermal correction can be expressed as follows [59]

$$V_T(v_\sigma, T) = \sum_S \frac{n_S T^4}{2\pi^2} J_B \left[ \frac{m_S^2(v_\sigma)}{T^2} \right] \quad (42)$$

where  $J_B$  is the thermal function for bosons

$$J_B = \int_0^\infty dx x^2 \log \left[ 1 - e^{-\sqrt{x^2 + m_S^2/T^2}} \right] \quad (43)$$

In finite-temperature field theory, when the temperature is high, the infrared amplitude of the fields becomes very large, leading to the breakdown of perturbative expansion. This problem is known as infrared divergence. To solve this problem, we need to perform daisy resummation on the free energy density. Daisy resummation resolves this issue by resumming the self-energy diagrams of the fields. There are usually two schemes for daisy resummation: the Arnold-Espinosa scheme [60] and the Parwani scheme [61]. In this work, we choose the Parwani scheme.  $\Pi_S^{ij}$  is the contribution of daisy resummation in thermal corrections. It can be expressed as follows [62]

$$\Pi_S^{ij} = \frac{T^2}{12} \sum_{k=1}^{n_{\text{scalars}}} L^{ijkk} \quad (44)$$

where  $n_{\text{scalars}}$  represents the number of scalar fields. Furthermore, the  $L^{ijkk}$  tensor can be defined as follows

$$\mathcal{L}_S = -L^i \Phi_i - \frac{1}{2!} L^{ij} \Phi_i \Phi_j - \frac{1}{3!} L^{ijk} \Phi_i \Phi_j \Phi_k - \frac{1}{4!} L^{ijkl} \Phi_i \Phi_j \Phi_k \Phi_l \quad (45)$$

The Lagrangian  $\mathcal{L}_S$  represents the model containing scalar fields  $\Phi_i$ , with  $i = h_u^R, h_u^0, \eta_u^0, h_d^I, h_d^0, \eta_d^0, \sigma^0, \eta_\sigma^0, h_u^I, h_d^R$ . The term  $L^{ijkl}$  denotes the coefficient corresponding to the interaction

term  $\Phi_i\Phi_j\Phi_k\Phi_l$ . The thermal corrections for the scalar fields are provided below

$$\begin{aligned}
\Pi_S^{00} &: \frac{20}{12} T^2 \lambda_1 + \frac{12}{12} T^2 \lambda_{12} + \frac{4}{12} T^2 \lambda_{13} + \frac{4}{12} T^2 \lambda_4 \\
\Pi_S^{11} &: \frac{11}{12} T^2 \lambda_1 + \frac{6}{12} T^2 \lambda_{12} + \frac{2}{12} T^2 \lambda_{13} + \frac{4}{12} T^2 \lambda_4 \\
\Pi_S^{22} &: \frac{11}{12} T^2 \lambda_1 + \frac{6}{12} T^2 \lambda_{12} + \frac{2}{12} T^2 \lambda_{13} + \frac{4}{12} T^2 \lambda_4 \\
\Pi_S^{33} &: \frac{20}{12} T^2 \lambda_2 + \frac{12}{12} T^2 \lambda_{12} + \frac{4}{12} T^2 \lambda_{23} + \frac{4}{12} T^2 \lambda_4 \\
\Pi_S^{44} &: \frac{11}{12} T^2 \lambda_2 + \frac{6}{12} T^2 \lambda_{12} + \frac{2}{12} T^2 \lambda_{23} + \frac{4}{12} T^2 \lambda_4 \\
\Pi_S^{55} &: \frac{11}{12} T^2 \lambda_2 + \frac{6}{12} T^2 \lambda_{12} + \frac{2}{12} T^2 \lambda_{23} + \frac{4}{12} T^2 \lambda_4 \\
\Pi_S^{66} &: \frac{3}{12} T^2 \lambda_3 + \frac{6}{12} T^2 \lambda_{23} + \frac{6}{12} T^2 \lambda_{13} \\
\Pi_S^{77} &: \frac{3}{12} T^2 \lambda_3 + \frac{6}{12} T^2 \lambda_{23} + \frac{6}{12} T^2 \lambda_{13} \\
\Pi_S^{88} &: \frac{20}{12} T^2 \lambda_1 + \frac{12}{12} T^2 \lambda_{12} + \frac{4}{12} T^2 \lambda_{13} + \frac{4}{12} T^2 \lambda_4 \\
\Pi_S^{99} &: \frac{20}{12} T^2 \lambda_2 + \frac{12}{12} T^2 \lambda_{12} + \frac{4}{12} T^2 \lambda_{23} + \frac{4}{12} T^2 \lambda_4
\end{aligned} \tag{46}$$

We calculate the field-dependent mass at finite temperature and subsequently perform the following substitution in the Parwani method [61]

$$m_S^2 \rightarrow \bar{m}_S^2 = m_S^2 + \Pi_S^{ij} \tag{47}$$

After obtaining the effective potential, we can use it to calculate some important phase transition parameters, such as the nucleation temperature, the characteristic length scale, the time scale of phase transition and phase transition strength. The characteristic length is the scale of the energy released during the phase transition, which is regarded as the mean bubble separation  $R$ . Typically, we utilize the time scale of phase transition  $\beta$  to estimate  $R$ , given by

$$R = \frac{(8\pi)^{1/3}}{\beta} v_w \tag{48}$$

where  $\beta$  is an approximation of the inverse time scale that plays a critical role in determining the shape of bubbles, and  $v_w$  is the bubble wall velocity. The bubble wall velocity is a crucial parameter in determining the spectra of phase transition GW which influences the strength and energy budget [63–67].  $\beta$  can be expressed as

$$\beta = - \left. \frac{d}{dt} \left( \frac{S_3(T)}{T} \right) \right|_{T=T_n} = H(T) T \left. \frac{d}{dT} \left( \frac{S_3}{T} \right) \right|_{T=T_n} \tag{49}$$

And the normalized parameter  $\beta_* = \frac{\beta}{H(T)}$ .  $T_n$  is the nucleation temperature.  $S_3$  represents the bounce action for a three-dimensional Euclidean space [68, 69],

$$S_3 = 4\pi \int_0^\infty dr r^2 \left[ \frac{1}{2} \left( \frac{dv_\sigma}{dr} \right)^2 + V_{\text{eff}}(v_\sigma, T) \right] \quad (50)$$

The nucleation rate per unit time and volume, represented by  $\Gamma$  [68], can be approximated as  $\Gamma \approx \Gamma_0 e^{-S_3}$ , where  $\Gamma_0$  is proportional to  $T^4$ . To calculate the bubble nucleation rate, we need to obtain the bubble profiles of  $v_\sigma$  by solving the bounce equation with the boundary conditions

$$\frac{d^2 v_\sigma}{dr^2} + \frac{2}{r} \frac{dv_\sigma}{dr} = \frac{\partial V_{\text{eff}}}{\partial v_\sigma}, \quad \left. \frac{dv_\sigma}{dr} \right|_{r=0} = 0, \quad v_\sigma|_{r=\infty} = v_{\sigma\text{false}} \quad (51)$$

where  $v_{\sigma\text{false}}$  is the scalar field value  $v_\sigma$  in the false vacuum. The overshooting/undershooting approach [70, 71] is commonly employed to solve the equation for the single-field bounce.  $T_n$  is the point at which the nucleation rate first surpasses the Hubble rate. More precisely, it is defined as follows

$$\frac{\Gamma(T_n)}{H(T_n)^4} = 1 \quad (52)$$

The Hubble rate  $H(T)$  during the radiation-dominated era is

$$H(T) = \left[ \left( \frac{\pi^2}{90} \right) g_* \right]^{1/2} \frac{T^2}{M_p} \quad (53)$$

where  $M_p$  is reduced Planck mass and  $g_*$  represents the effective number of relativistic *d.o.f.*. Within the bag model framework, the phase transition strength parameter  $\alpha$  is typically defined as [72]

$$\alpha = \left. \frac{\Delta V_{\text{eff}} - T \frac{\partial \Delta V_{\text{eff}}}{\partial T}}{\rho_R} \right|_{T=T_n} \quad (54)$$

To derive  $\alpha$ , we can utilize the expressions for the effective potential  $V_{\text{eff}}$  and its derivative concerning  $T_n$ , respectively. The effective energy density  $\rho_R$  can be expressed as  $\rho_R = \frac{\pi^2 g_* T_n^4}{30}$ .  $\Delta V_{\text{eff}}$  refers to the difference in effective potential between the symmetric phase and the broken phase at  $T_n$ .

The GW spectrum, which is generated by three primary processes: bubble collisions, sound waves in the plasma, and turbulence, can be accurately calculated by using these key phase transition parameters derived from the effective potential.

- Bubbles collisions

According to the envelope approximation, the shape of the uncollided bubble walls is

the key factor determining the generation of GWs. Based on the numerical simulation, we obtain [18–22]

$$h_{100}^2 \Omega_{\text{co}}(f) \simeq 1.67 \times 10^{-5} \left( \frac{H_* R}{(8\pi)^{1/3}} \right)^2 \left( \frac{\kappa_\sigma \alpha}{1 + \alpha} \right)^2 \left( \frac{100}{g_*} \right)^{1/3} \frac{0.11 v_w}{0.42 + v_w^2} \frac{3.8 (f/f_{\text{co}})^{2.8}}{1 + 2.8 (f/f_{\text{co}})^{3.8}} \quad (55)$$

where  $\kappa_\phi$  represents the fraction of vacuum energy converted into the gradient energy of the scalar field, and  $H_*$  is the Hubble parameter at  $T_n$ . The peak frequency of the GW spectrum generated by bubble collisions is given by

$$f_{\text{co}} \simeq 1.65 \times 10^{-5} \text{ Hz} \frac{(8\pi)^{1/3}}{H_* R} \left( \frac{0.62 v_w}{1.8 - 0.1 v_w + v_w^2} \right) \left( \frac{T_n}{100 \text{ GeV}} \right) \left( \frac{g_*}{100} \right)^{1/6} \quad (56)$$

- Sound wave

The expansion of bubbles leads to the formation of sound waves in the surrounding fluid. Based on the numerical simulation, we obtain [23, 24]

$$h_{100}^2 \Omega_{\text{sw}}(f) \simeq 2.65 \times 10^{-6} \beta^{-1} \left( \frac{\kappa_{\text{sw}} \alpha}{1 + \alpha} \right)^2 \left( \frac{100}{g_*} \right)^{1/3} v_w (f/f_{\text{sw}})^3 \left( \frac{7}{4 + 3 (f/f_{\text{sw}})^2} \right)^{7/2} \quad (57)$$

where  $\kappa_{\text{sw}}$  represents the fraction of vacuum energy that is converted into the kinetic energy of the fluid's bulk motion and the peak frequency of the GW spectrum generated by sound wave is given by

$$f_{\text{sw}} \simeq 2.6 \times 10^{-5} \text{ Hz} \frac{1}{H_* R} \left( \frac{T_n}{100 \text{ GeV}} \right) \left( \frac{g_*}{100} \right)^{1/6} \quad (58)$$

- Turbulence

As the fluid propagates, the complex physical process of turbulence can be triggered. Based on the numerical simulation, we obtain [25, 26]

$$h_{100}^2 \Omega_{\text{turb}}(f) \simeq 1.14 \times 10^{-4} H_* R \left( \frac{\kappa_{\text{turb}} \alpha}{1 + \alpha} \right)^{3/2} \left( \frac{100}{g_*} \right)^{1/3} \frac{(f/f_{\text{turb}})^3}{(1 + f/f_{\text{turb}})^{11/3} (1 + 8\pi f/H_*)} \quad (59)$$

where  $\kappa_{\text{turb}}$  represents how effectively vacuum energy is converted into turbulent flow

$$\kappa_{\text{turb}} = \tilde{\epsilon} \kappa_{\text{sw}} \quad (60)$$

We chose  $\tilde{\epsilon} = 0.1$  and the peak frequency of the GW spectrum generated by turbulence is given by

$$f_{\text{turb}} \simeq 7.91 \times 10^{-5} \text{ Hz} \frac{1}{H_* R} \left( \frac{T_*}{100 \text{ GeV}} \right) \left( \frac{g_*}{100} \right)^{1/6} \quad (61)$$

TABLE I. Four sets benchmark parameters of DFSZ-I model

	$\mu_3$ [GeV]	$\lambda_3$	$\lambda_{13}$	$\lambda_{23}$	$\mu$ [GeV]	$T_n$ [GeV]	$v_\sigma(T_n)$ [GeV]	$\alpha$	$\beta^*$
$BP_1$	$7.13 \times 10^5$	$1.19 \times 10^{-4}$	1.91	0.70	$1.12 \times 10^6$	$1.34 \times 10^7$	$3.31 \times 10^7$	0.87	330
$BP_2$	$6.13 \times 10^6$	$1.12 \times 10^{-3}$	1.79	0.59	$2.69 \times 10^6$	$1.02 \times 10^7$	$2.55 \times 10^7$	0.81	586
$BP_3$	$7.13 \times 10^5$	$1.66 \times 10^{-3}$	0.91	0.70	$3.15 \times 10^6$	$9.76 \times 10^6$	$4.06 \times 10^7$	1.63	579
$BP_4$	$6.13 \times 10^5$	$1.20 \times 10^{-4}$	1.90	0.60	$1.35 \times 10^6$	$1.36 \times 10^7$	$3.50 \times 10^7$	0.67	936

To find the parameter space that can generate a strong phase transition, we performed numerical calculations on the phase transition dynamics by using the CosmoTransitions package [73]. We aim for the phase transition to occur at a high energy scale to generate strong GW signals. So during the calculations, we imposed the following optimization conditions on the parameters: the critical temperature  $T_c$  should be as high as possible and at least greater than the electroweak scale 100 GeV;  $v_\sigma$  should significantly exceed 246 GeV since the vev is related to the energy scale of the phase transition; and the ratio of the scalar field mass to the nucleation temperature should be much smaller than 1 to ensure the applicability of perturbation expansion in Eq. (43). By systematically scanning the parameter space and obtaining results that maximize these conditions, we obtained several parameter combinations that have a high-energy scale. We present four benchmark parameter sets ( $BP_1$ ,  $BP_2$ ,  $BP_3$ , and  $BP_4$ ) for the DFSZ-I model in Tab. I. These sets are selected based on two main criteria: (1) consistency with the current experimental constraints on the axion-photon coupling,  $g_{a\gamma\gamma}$ , and (2) the ability to generate a SFOPT with high-energy scale. These parameter sets will be used to calculate the GW spectra. Then be compared with the sensitivity curves of the CE and ET detectors to determine whether these detectors can observe the GW signals predicted by this model. During the calculations, we find some parameters have a relatively smaller impact on the resulting phase transition GW signals. For simplicity, these model parameters  $\lambda_1$ ,  $\lambda_4$ , and  $\lambda_{12}$  are fixed at 0.0001,  $\lambda_2$  is set to 0.1, and  $\mu_1$  and  $\mu_2$  are fixed at  $6 \times 10^5$  GeV. The remaining model parameters, including  $\mu_3$ ,  $\lambda_3$ ,  $\mu$ ,  $\lambda_{13}$ , and  $\lambda_{23}$ , are varied to generate different phase transition parameters.

We obtained phase transitions with energy scales up to  $f_{PQ} = v_\sigma(T_n) = 40$  PeV, where

TABLE II. Axion mass,  $g_{a\gamma\gamma}$  for different  $f_{PQ}$  values.

	$f_{PQ}$ [GeV]	$m_a$ [eV]	$g_{a\gamma\gamma}$ [GeV $^{-1}$ ]
$BP_1$	$3.31 \times 10^7$	0.17	$5.17 \times 10^{-10}$
$BP_2$	$2.55 \times 10^7$	0.22	$6.71 \times 10^{-10}$
$BP_3$	$4.06 \times 10^7$	0.14	$4.22 \times 10^{-10}$
$BP_4$	$3.50 \times 10^7$	0.16	$4.89 \times 10^{-10}$

$f_{PQ}$  is the PQ symmetry-breaking scale. Since the axion mass is inversely proportional to  $f_{PQ}$  [74], the high-energy scale result indicates that it may be possible for invisible axions to exist in the DFSZ-I model.

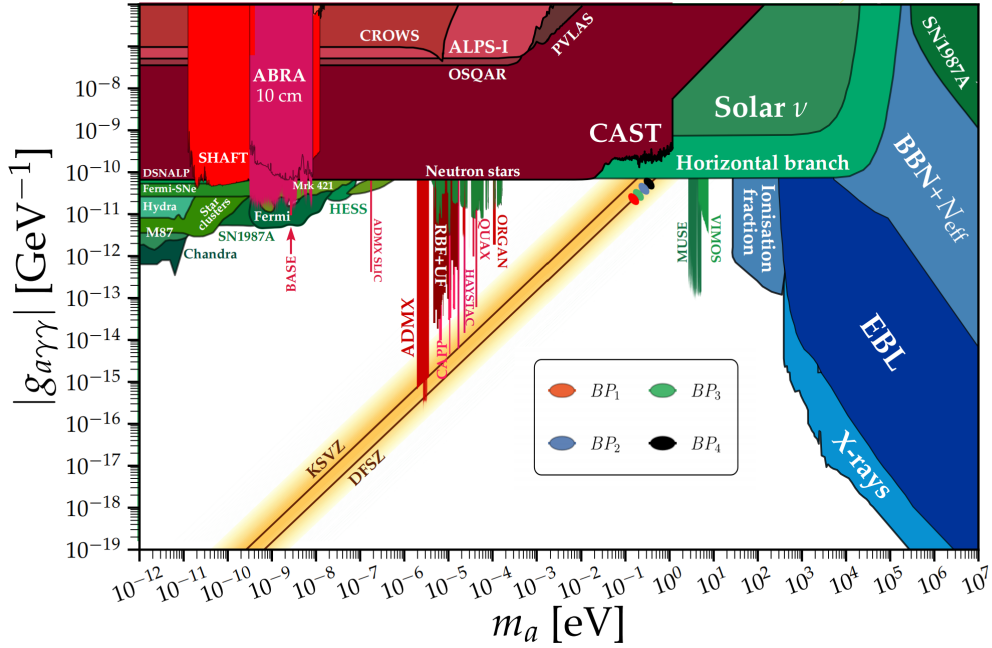


FIG. 1. The  $m_a$  and  $g_{a\gamma\gamma}$  obtained from all four benchmark points in the ALP-photon coupling exclusion diagram from [76].

$$m_a = 5.691(51) \left( \frac{10^9 \text{ GeV}}{f_{PQ}} \right) \text{ meV} \quad (62)$$

The numbers in parentheses represent the uncertainty in the last two digits of the main value. Given the  $m_a$ , we can calculate the axion-photon coupling constant  $g_{a\gamma\gamma}$ . The calculation as follows [75]

$$g_{a\gamma\gamma} = \frac{\alpha_c}{2\pi f_{PQ}} \left( \frac{E}{N} - 1.92(4) \right) = \left( 0.203(3) \frac{E}{N} - 0.39(1) \right) \frac{m_a}{\text{GeV}^2} \quad (63)$$

where  $\alpha_c$  is the fine structure constant,  $E/N$  is the ratio of the electromagnetic anomaly coefficient to the colour anomaly coefficient. For the DFSZ-I model,  $E/N$  is  $8/3$  [7, 8].

Figure 1 shows the ALP-photon coupling exclusion plot. The coloured regions represent the excluded parameter space from various ALP-photon coupling experiments, such as CAST, ADMX, etc. The yellow band denotes the theoretically predicted range for axions. The four elliptical points  $BP_{1-4}$  in the plot represent four benchmark parameter sets in Tab.I, which are shown in red, blue, green, and black, respectively. The corresponding  $m_a$  and  $g_{a\gamma\gamma}$  values for these points are listed in Table II. The  $m_a$  for  $BP_1$ ,  $BP_2$ ,  $BP_3$ , and  $BP_4$  is 0.17 eV, 0.22 eV, 0.14 eV, and 0.16 eV, respectively. All four points fall within the expected yellow region showing that these points satisfy the constraints from existing experiments. This result identifies parameter sets that are consistent with experimental constraints and the ability to achieve high-energy scale SFOPT.

Figure 2 shows the GW spectrum for four benchmark parameter sets. The light-green and orange curves represent the sensitivity curves for ET and CE with SNR=1 (more details of the sensitivity curves for detectors will be introduced in the next section), respectively, over a running time of  $1 \times 10^8$  s. The red, blue, green, and black curves represent the GW signals for  $BP_1$ ,  $BP_2$ ,  $BP_3$ , and  $BP_4$  with the  $v_w = 0.9$ . The SNR values using the definition of Eq. (27) for each benchmark point are

$$SNR : \quad BP_1(93.26) \quad BP_2(14.34) \quad BP_3(29.12) \quad BP_4(0.77) \quad (64)$$

Table III shows that the SNR of  $BP_4$  is only 0.77, which is significantly below the threshold value SNR=8 [30] for the CE detector, making its signal difficult to capture by the CE detector.  $BP_1$  has an SNR of 93.26,  $BP_2$  has an SNR of 14.34 and  $BP_3$  has an SNR of 29.12. The SNR values of these three curves exceed the threshold, indicating that the CE detector can detect them. The detectability of  $BP_1$ ,  $BP_2$ , and  $BP_3$  indicates that the DFSZ-I model can generate observable axion phase transition GW signals.

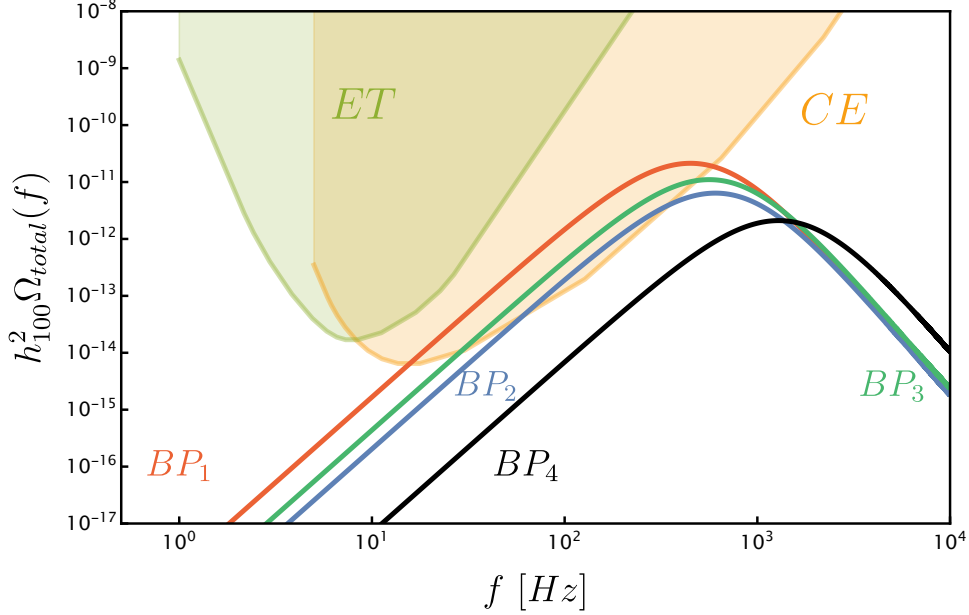


FIG. 2. GW spectra for DFSZ-I model. The light-green and orange curves depict the sensitivity curves with SNR=1 for ET and CE, respectively. The red, blue, green, and black curves represent the phase transition GW signals for  $BP_1$ ,  $BP_2$ ,  $BP_3$ , and  $BP_4$  with  $v_w = 0.9$ . The relevant parameters are summarized in Tab. I.

To investigate the impact of the unknown parameter  $v_w$  on the GW spectrum, we consider two representative values which may produce stronger GW signals during the phase transition process:  $v_w = 0.92$  and  $v_w = 0.8$ . Fig. 3 shows the GW spectrum for two benchmark parameter sets  $BP_1$  and  $BP_3$  that have higher SNR with different  $v_w$ .  $BP_1$  (red solid line) and  $BP_1$  (red dash-dotted line) correspond to the expected GW signals of  $v_w = 0.92$  and  $v_w = 0.8$ , respectively.  $BP_3$  (green solid line) and  $BP_3$  (green dash-dotted line) correspond to the expected GW signals of  $v_w = 0.92$  and  $v_w = 0.8$ , respectively. We find that there are differences in the frequency and strength of the GW spectra under different  $v_w$  values in Fig. 3. In order to assess the constraining power of CE on these phase transition parameters more precisely, we need to quantify the uncertainties of each parameter. FM analysis is a powerful statistical tool which is widely used for estimating the precision of parameter estimates. In the next section, we will use FM analysis to calculate the relative uncertainties of the phase transition parameters in the DFSZ-I model and evaluate the constraining power of CE on these parameters.

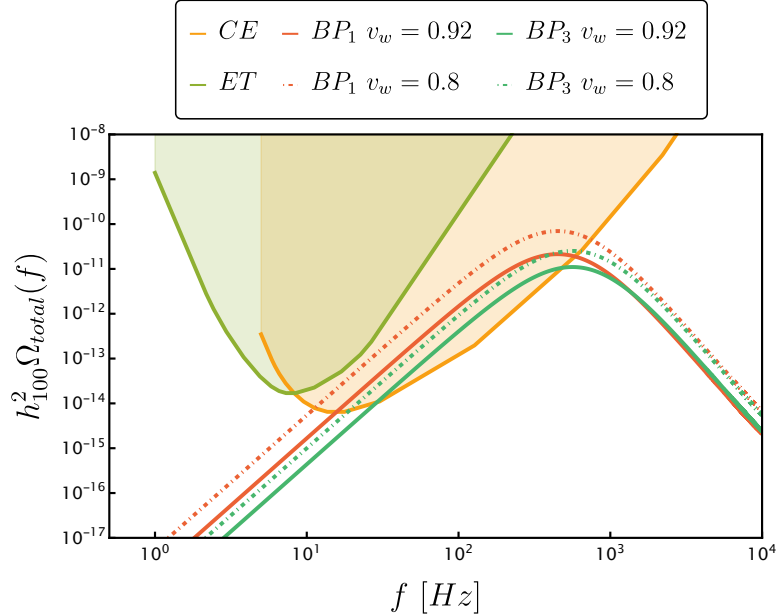


FIG. 3. GW spectra for DFSZ-I model with  $v_w = 0.92$  and  $v_w = 0.8$ . The light-green and orange curves depict the sensitivity curves with SNR=1 for ET and CE.  $BP_1$  (red solid line) and  $BP_1$  (red dash-dotted line) correspond to the expected GW signals of  $v_w = 0.92$  and  $v_w = 0.8$ , respectively.  $BP_3$  (green solid line) and  $BP_3$  (green dash-dotted line) correspond to the expected GW signals of  $v_w = 0.92$  and  $v_w = 0.8$ , respectively. The relevant parameters are summarized in Tab. I.

TABLE III. SNR values for two benchmark parameter sets at three different bubble wall velocities  $v_w$ .

	$v_w = 0.92$	$v_w = 0.9$	$v_w = 0.8$
$BP_1$	102.26	93.26	56.83
$BP_3$	31.98	29.12	17.60

## V. FISHER MATRIX ANALYSIS OF THE PHASE TRANSITION PARAMETER AT COSMIC EXPLORER

FM is a powerful statistical tool which is widely used for estimating the precision of parameter estimates in various fields, including GW astronomy [33]. For a probability distribution  $f(x; \Theta)$ , of an observable random variable  $x$  that depends on a set of unknown parameters  $\Theta = (\Theta_1, \dots, \Theta_k)$ , the FM is defined as the expected value of the second-order

partial derivatives of the log-likelihood function with respect to the parameters. One of the critical properties of the FM is that the inverse of the FM corresponds to the covariance matrix of the observable parameters as the probability distribution approximates a Gaussian distribution [77]. The diagonal elements of the inverse FM are the variances (squared uncertainties) of the parameter estimates. Therefore, smaller values of these diagonal elements indicate more precise parameter estimates with lower uncertainties. We will use FM analysis to calculate the relative uncertainties of phase transition parameters, which enables us to assess the constraining power of detectors such as the CE and ET on these parameters. To apply FM analysis, we first need to construct a likelihood model for CE.

### A. Likelihood model

In our study, the observational data is the GW signal detected by CE, and the theoretical model parameters are the dynamical parameters of the phase transition generated by the DFSZ-I axion model. In the following discussion, we will introduce in detail how to construct the likelihood model using CE, in preparation for the subsequent FM analysis.

The GW strain in the frequency domain,  $\tilde{h}_{gw}(f_n)$ , is given by the discrete Fourier transform of the time-domain strain,  $h_{gw}(t)$  [78]

$$\tilde{h}_{gw}(f_n) = \frac{1}{\sqrt{N_t}} \sum_{m=0}^{N_t-1} h_{gw}(t_m) \exp(-2\pi i f_n t_m) \quad (65)$$

where  $N_t = T_{tot}/T_s$  is the total number of samples,  $T_{tot} = 1 \times 10^8$  s is the total observation time for the CE mission, and  $T_s$  is the data sampling period. The time  $t_m$  is given by  $t_m = mT_s$ , where  $m$  is an integer ranging from  $-N_t/2$  to  $N_t/2$ . The frequency  $f_n$  is defined as

$$f_n = n/T_{tot} \quad (66)$$

where  $n$  is an integer ranging from  $-N_t/2$  to  $N_t/2$ . The GW energy density spectrum,  $\Omega_{gw}(f_n)$ , is related to the strain in the frequency domain by

$$\Omega_{gw}(f_n) = \left( \frac{4\pi^2}{3H_0^2} \right) f_n^2 \left| \tilde{h}_{gw}(f_n) \right|^2 \quad (67)$$

The PSD of the CE detector can be expressed as  $E_n$  and the variances of the Fourier amplitudes are denoted as  $A_n$ . To optimize computational efficiency, we employ a simplified

approach for data grouping known as frequency binning. This involves dividing the frequency range into  $N_b$  bins, where the spacing between consecutive bins follows a logarithmic scale. Consequently, each bin contains a specific number of frequencies, denoted as  $n_b$

$$n_b = [(f_b - f_{b-1}) T_{\text{tot}}], 0 \leq b \leq N_b \quad (68)$$

where  $f_b$  and  $f_{b-1}$  are the upper and lower frequency boundaries of the  $b$ -th bin. The relationship between  $A_n$  and  $E_n$  can be expressed as

$$\bar{E}_n = \frac{A_b}{n_b} \sum_{n \in I_b} \frac{E_n}{A_n} \quad (69)$$

with

$$\frac{1}{A_b} = \frac{1}{n_b} \sum_{n \in I_b} \frac{1}{A_n} \quad (70)$$

$A_b$  is the mean value of the distribution. Let  $I_b$  denote a group of integers numbers. Consider a set of independent normal random variables  $A_1, \dots, A_n$ , the variable

$$\sum_{n \in I_b} \frac{E_n}{A_n} = E_1/A_1 + \dots + E_n/A_n \quad (71)$$

approximates a Gamma distribution with shape parameter  $2n_b$  when  $n_b$  is sufficiently large, according to the Central Limit Theorem. This distribution arises from scaling the Chi-square distribution

$$p(\bar{E}_b | A_b) = \prod_{b=1}^{N_b} \frac{1}{(n_b - 1)!} \frac{n_b}{A_b} \left( n_b \frac{\bar{E}_b}{A_b} \right)^{n_b - 1} \exp\left(-n_b \frac{\bar{E}_b}{A_b}\right) \quad (72)$$

Under the Gaussian approximation, we have

$$p(\bar{E}_b | A_b) = \prod_{b=1}^{N_b} \left( \frac{n_b}{2\pi A_b^2} \right)^{\frac{1}{2}} \exp\left(-\frac{1}{2} \frac{n_b (\bar{E}_b - A_b)^2}{A_b^2}\right) \quad (73)$$

From Eq. (C1) in the Appendix, the natural logarithm of the likelihood function with the Gaussian approximation is

$$l_G = \ln(p) = -\frac{1}{2} \sum_{b=1}^{N_b} \frac{n_b (\bar{E}_b - A_b)^2}{A_b^2} - \sum_{b=1}^{N_b} \ln 2A_b + \text{const.} \quad (74)$$

The FM can be obtained from Eq. (C7) is

$$\begin{aligned}
F_{ij}^G &= E \left[ \frac{\partial l_G}{\partial \Theta_i} \frac{\partial l_G}{\partial \Theta_j} \right] \\
&= E \left[ \frac{\partial l_G}{\partial A_b} \frac{\partial l_G}{\partial A_b} \frac{\partial A_b}{\partial \Theta_i} \frac{\partial A_b}{\partial \Theta_j} \right] \\
&= E \left[ \frac{\partial^2}{\partial^2 A_b} \left( -\frac{1}{2} \sum_{b=1}^{N_b} \frac{n_b (\bar{E}_b - A_b)}{A_b^2} - \sum_{n=1}^{N_b} \ln 2A_b \right) \right] \frac{\partial A_b}{\partial \Theta_i} \frac{\partial A_b}{\partial \Theta_j} \\
&= \sum_{b=1}^{N_b} \frac{n_b}{A_b^2} \frac{\partial A_b}{\partial \Theta_i} \frac{\partial A_b}{\partial \Theta_j} \\
&= T_{\text{obs}} \sum_{b=1}^{N_b} \frac{\Delta f_b}{\Omega_t^2} \frac{\partial \Omega_t}{\partial \Theta_i} \frac{\partial \Omega_t}{\partial \Theta_j}
\end{aligned} \tag{75}$$

To establish the theoretical model for the data, we will employ the total power spectrum  $\Omega_t$  (defined in Eq. (84)) instead of the spectral densities  $A_b$ . The covariance matrix is the inverse of the FM, and the square roots of the diagonal entries correspond to the relative uncertainties of the parameters.

## B. Cosmic Explorer noise

The CE and the ET are third-generation ground-based GW detectors, anticipated to commence operations post-2030 [27–32]. In comparison to second-generation detectors, their sensitivity is expected to increase by an order of magnitude, enabling the detection of frequencies as low as several hertz. This sensitivity enhancement will allow for the observation of  $\mathcal{O}(10^5\text{-}10^6)$  compact binary coalescence events (CBCs) within a year-long observation period, not limited to binary black hole (BBH) and binary neutron star (BNS) mergers. As shown in Fig. 2, CE can detect GW signals from SFOPT in axion models. Therefore, we choose CE as an example to perform FM analysis. To better understand the noise model of CE, we need to carefully analyze various noise sources and their impact on the detector’s sensitivity.

### 1. shot noise

The first noise source we consider is the shot noise of the laser, stemming from the quantum nature of photons. In GW detectors, shot noise limits the sensitivity at high

frequencies. One method to mitigate the impact of shot noise on experimental results is increasing the number of photons received by the detector, achievable by amplifying the power of the beam,  $P_{\text{bs}}$ . The initial beam power,  $P_0$ , refers to the power of the original beam from the laser source incident on the interferometer. A beam splitter is an optical component that divides an incoming beam into two parts, and  $C$  represents the multiplier by which the beam power is increased before reaching the beam splitter. Therefore,  $P_{\text{bs}} \equiv CP_0 = 1650 \text{ kw}$  denotes the power measured at the beam splitter after power amplification.

The shot noise is formulated as [55]

$$S_n^{1/2}(f)|_{\text{shot}} = \frac{1}{8\mathcal{F}L} \left( \frac{4\pi\hbar\lambda_L c}{\eta P_{\text{bs}}} \right)^{1/2} \sqrt{1 + (f/f_p)^2} \quad (76)$$

where  $\mathcal{F}$  denotes the Finesse of the Fabry-Perot cavities, a measure of the optical quality and reflectivity of the mirrors within the Fabry-Perot interferometer, set at  $\mathcal{F} = 200$ .  $L$  is arm lengths of 40 km and  $\eta = 0.96$  is the efficiency of the photodetector. The pole frequency,  $f_p = 500 \text{ Hz}$ , is a crucial parameter describing the frequency response of a GW detector, especially those utilizing Fabry-Perot cavities. The symbol  $\lambda_L$  denotes the laser wavelength used in the interferometer, which is approximately 1550 nm.

## 2. radiation pressure

In GW detection, enhancing the experimental signal through increased laser beam power is a common practice [79]. However, while this approach improves detector sensitivity, it also introduces additional noise in the form of radiation pressure. This pressure is the movement of mirrors as the beam traverses its path and reflects, exerting a force on the mirrors in the system. At high frequencies, shot noise typically dominates over radiation pressure noise, while at low frequencies, radiation pressure noise becomes more significant. The strain sensitivity due to radiation pressure typically takes the following form [55]

$$S_n^{1/2}(f)|_{\text{rad}} = \frac{16\sqrt{2}\mathcal{F}}{ML(2\pi f)^2} \sqrt{\frac{\hbar}{2\pi} \frac{P_{\text{bs}}}{\lambda_L c}} \frac{1}{\sqrt{1 + (f/f_p)^2}} \quad (77)$$

where  $M = 320 \text{ kg}$  represents the mass of the mirror.

Combining the shot noise and radiation pressure, one obtains the optical readout noise with its PSD given by

$$S_n(f)|_{\text{opt}} = S_n(f)|_{\text{shot}} + S_n(f)|_{\text{rad}} \quad (78)$$

So that the energy density is

$$\Omega_{\text{opt}} = \left( \frac{4\pi^2}{3H_0^2} \right) f^3 S_n(f)|_{\text{opt}} \quad (79)$$

### 3. Seismic noise

Seismic noise arises from the continuous movement of the ground, with amplitudes around several micrometres. The strain sensitivity due to seismic noise typically can be represented as [55]

$$\frac{x(f)}{L} \simeq \frac{A}{L} \left( \frac{1 \text{ Hz}}{f} \right)^\nu \text{ m} \cdot \text{Hz}^{-1/2} \quad (80)$$

Above 1 Hz, the exponent  $\nu \simeq 2$ , with the magnitude of  $A$  around  $10^{-7}$ . Dividing  $x(f)$  by the length  $L$ , we obtain the noise strain sensitivity. The energy density is

$$\Omega_{\text{se}} = \left( \frac{4\pi^2}{3H_0^2} \right) f^3 \left( \frac{x(f)}{L} \right)^2 \quad (81)$$

Seismic noise predominantly governs the lower frequency domain, while at higher frequencies, shot noise and radiation pressure noise become increasingly significant. The total power spectrum energy density of the CE noise model is

$$\Omega_{\text{n}} = \Omega_{\text{opt}} + \Omega_{\text{se}} \quad (82)$$

### 4. Compact binary coalescence

The GW power spectrum of CBCs foreground, such as BBH and BNS [80–82] is often defined as

$$\Omega_{\text{cbc}}(f) = \Omega_{\text{ref}} \left( \frac{f}{f_{\text{ref}}} \right)^{2/3} \quad (83)$$

where  $\Omega_{\text{ref}}$  represents the energy spectral density at a reference frequency  $f_{\text{ref}}$ . Due to the uncertain spatial distribution of BBH and BNS sources,  $\Omega_{\text{ref}}$  is uncertain, typically ranging from  $10^{-7}$  to  $10^{-10}$  [82]. For this analysis, we assume  $\Omega_{\text{ref}} = 10^{-10}$ . For BBH mergers, which typically occur within a frequency range from a few hertz to several hundred hertz, we set a reasonable reference frequency  $f_{\text{ref}} = 200$  Hz. This frequency is indicative of the coalescence phase during the BBH merger process, where the GW signal is at its strongest. For BNS mergers, which happen at slightly higher frequencies compared to BBH mergers, a higher reference frequency of 1000 Hz is selected.

The total energy density is

$$\Omega_t = \Omega_n + \Omega_{\text{cbc}} + \Omega_{\text{gw}} \quad (84)$$

### C. The relative uncertainties

After obtaining Eq. (84) for the CE detector, we can substitute it into Eq. (75) to calculate the relative uncertainty of specific GW model parameters. We choose the sound wave mechanism, which dominates the GW spectrums. The considered parameters include the phase transition strength, Hubble-scaled mean bubble separation  $R_H = H_* R$ , and nucleation temperature. These parameters can be encapsulated in a vector  $\vec{\Theta}$ , defined as  $\vec{\Theta} = (v_w, \alpha, R_H, (T_n/\text{GeV}))$ . To calculate the relative uncertainties of the GW spectrum generated by the sound wave mechanism, we rewrite Eq. (57) in the following form to include the  $R_H$

$$h_{100}^2 \Omega_{sw}(f) \cong 1.64 \times 10^{-6} \frac{R_H^2}{\bar{U}_f} \left( \frac{\kappa_v \alpha}{1 + \alpha} \right)^2 \left( \frac{100}{g_*} \right)^{1/3} \left( \frac{f}{f_{sw}} \right)^3 \left( \frac{7}{4 + 3(f/f_{sw})^2} \right)^{7/2} \quad (85)$$

$$f_{sw} \cong 2.6 \times 10^{-5} \text{ Hz} \frac{1}{R_H} \left( \frac{T_n}{100 \text{ GeV}} \right) \left( \frac{g_*}{100} \right)^{1/6} \quad (86)$$

$$\bar{U}_f^2 \approx \frac{3}{4} \frac{\kappa_v \alpha}{1 + \alpha} \quad (87)$$

We have selected a set of phase transition parameters around  $BP_1$  from Tab.I that can be detected by CE. We set  $T_n$  to be  $1.34 \times 10^7$  GeV and  $R_H = 0.1$ . The parameter space is sampled by varying  $v_w$  from 0.92 to 0.94 and  $\alpha$  from 0.58 to 0.65.

Figure 4 contains four subplots, each showing the relative uncertainties of  $v_w$ ,  $\alpha$ ,  $R_H$ , and  $T_n$  within the given ranges of  $v_w$  and  $\alpha$ :  $\Delta v_w/v_w$ ,  $\Delta \alpha/\alpha$ ,  $\Delta R_H/R_H$ , and  $\Delta T_n/T_n$ . A colour bar on the right side of the figure indicates the magnitude of the relative uncertainties. From dark blue to light green, the relative uncertainties gradually increase. It can be seen from the figure that the relative uncertainty of  $v_w$  is the smallest, as the colour in the  $v_w$  subplot is the most blue-shifted. These results indicate that detectors like CE will be most sensitive to and place the strongest constraints on measurements of the  $v_w$ . The results obtained through the FM analysis are consistent with the findings presented in Fig. 3.

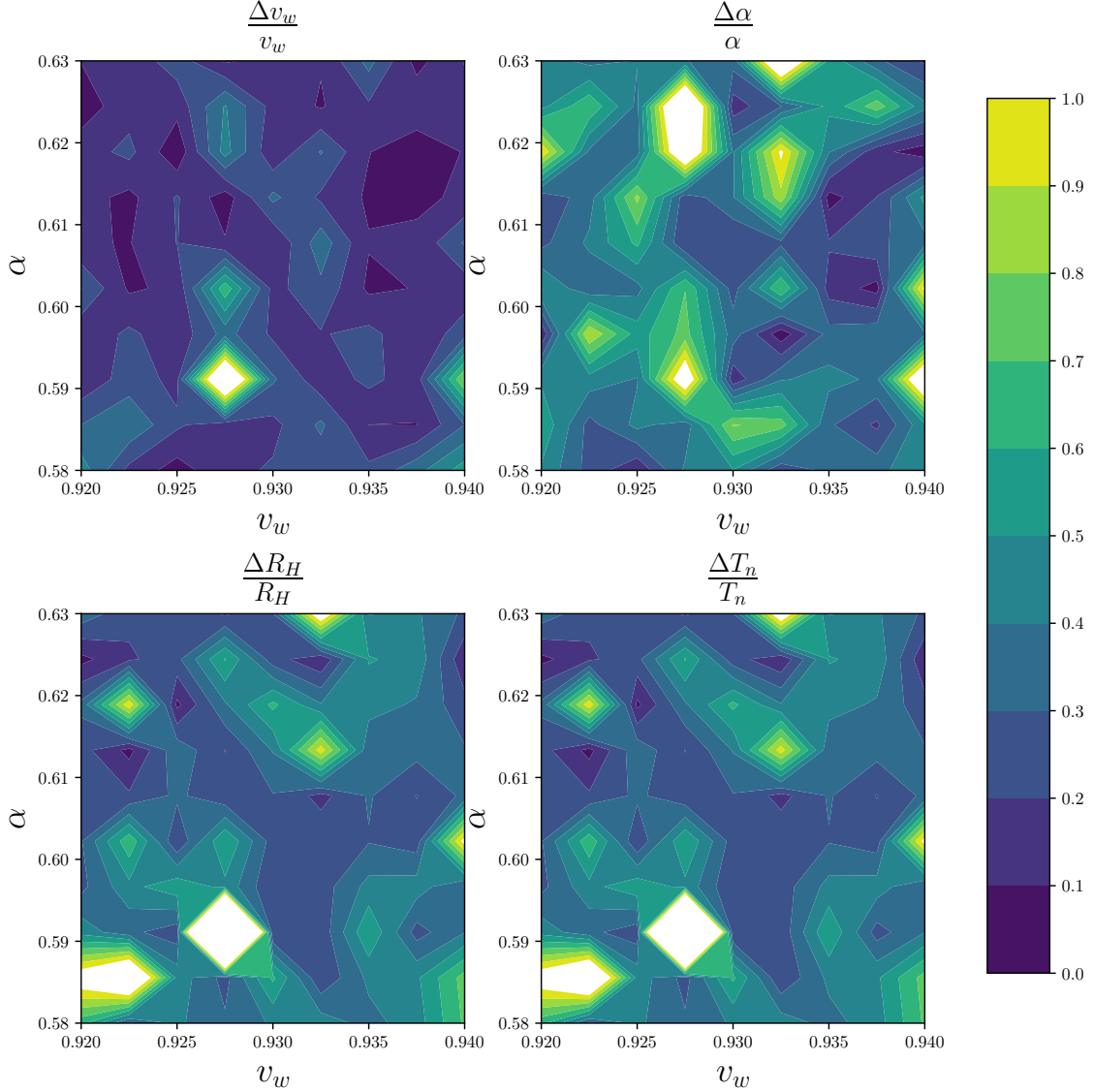


FIG. 4. Relative uncertainty with phase transition dynamics parameters wall speed  $v_w$ , transition strength  $\alpha$ , Hubble-scaled mean bubble spacing  $R_H$ , and nucleation temperature  $T_n$ .

## VI. DISCUSSIONS AND CONCLUSION

We have investigated GW detection of the DFSZ axion model at CE. Taking the popular DFSZ-I axion model as a typical example, we precisely calculate the phase transition dynamics of the U(1) PQ symmetry-breaking process and its associated phase transition GW. After scanning different model parameter combinations in the DFSZ-I model, we find that the U(1) PQ symmetry-breaking can be the cosmological SFOPT at high energy scales up to 40 PeV that current experiments are unable to reach. We calculate the axion mass

and axion-photon coupling constant predicted by the DFSZ model and compare them with current experimental constraints to find the benchmark points. We find that the parameters can not only generate a SFOPT with a high-energy scale but also are consistent with the current experimental constraints on the axion-photon coupling. Then, we quantified the detectability of the DFSZ-I model at the CE and ET by precisely calculating the SNR. For  $v_w = 0.9$ , three signals achieve  $SNR > 8$  at CE, indicating that they can be observed by CE.

Considering the uncertainty of GW spectra from the bubble wall velocity, we provide GW spectra under different bubble wall velocities as examples. The results show that the GW spectrum is sensitive to the value of the bubble wall velocity. Based on this, to further quantify the uncertainties of phase transition parameters at future GW detectors, we perform FM analysis on the key phase transition parameters, including  $v_w$ ,  $\alpha$ ,  $R_H$ , and  $T_n$ . The results show that the relative uncertainty of  $v_w$  is smaller than the relative uncertainties of other parameters. Thus, if the predicted phase transition GW spectra are observed at detectors like CE, bubble wall velocity  $v_w$  will be the first parameter to be measured or most strongly constrained.

Looking ahead, the construction and operation of next-generation GW detectors such as ET and CE are expected to improve the ability to detect phase transition GW. This study demonstrates that CE detectors have the potential to detect GWs from the U(1) PQ symmetry-breaking process, providing a novel approach to probe the existence of axion. More comprehensive studies in various axion models are left in our future studies.

## ACKNOWLEDGMENTS

We thank Seokhoon Yun for the helpful discussions on axion constraints and Siyu Jiang for making useful suggestions on the manuscript. This work is supported by the National Natural Science Foundation of China (NNSFC) under Grant No.12205387. This work is partly supported in part by Guangdong Major Project of Basic and Applied Basic Research (Grant No. 2019B030302001).

## Appendix A: The field-dependent mass

To determine the field-dependent mass of each physical particle, we need to diagonalize the mass-squared matrix. The elements of the mass-squared matrix  $M$  for the bosons can be expressed as follows

$$\begin{aligned}
 M_{00} &= v_\sigma^2 \lambda_{13} - 2\mu_1^2, & M_{11} &= \frac{v_\sigma^2 \lambda_{13}}{2} - \mu_1^2, & M_{22} &= \frac{v_\sigma^2 \lambda_{13}}{2} - \mu_1^2 \\
 M_{33} &= v_\sigma^2 \lambda_{23} - 2\mu_2^2, & M_{44} &= \frac{v_\sigma^2 \lambda_{23}}{2} - \mu_2^2, & M_{55} &= \frac{v_\sigma^2 \lambda_{23}}{2} - \mu_2^2 \\
 M_{66} &= 3v_\sigma^2 \lambda_3 - \mu_3^2, & M_{77} &= v_\sigma^2 \lambda_3 - \mu_3^2, & M_{88} &= v_\sigma^2 \lambda_{13} - 2\mu_1^2 \\
 M_{99} &= v_\sigma^2 \lambda_{23} - 2\mu_2^2, & M_{03} &= -v_\sigma^2 \lambda_5, & M_{30} &= -v_\sigma^2 \lambda_5 \\
 M_{14} &= \frac{v_\sigma^2 \lambda_5}{2}, & M_{41} &= \frac{v_\sigma^2 \lambda_5}{2}, & M_{25} &= -\frac{v_\sigma^2 \lambda_5}{2} \\
 M_{52} &= -\frac{v_\sigma^2 \lambda_5}{2}, & M_{89} &= \frac{v_\sigma^2 \lambda_5}{2}, & M_{98} &= \frac{v_\sigma^2 \lambda_5}{2}
 \end{aligned}$$

Let

$$G_{44} = M_{44} + \Pi_S^{44}, \quad G_{55} = M_{55} + \Pi_S^{55}, \quad G_{66} = M_{66} + \Pi_S^{66} \quad (\text{A1})$$

$$G_{77} = M_{77} + \Pi_S^{77}, \quad G_{88} = M_{88} + \Pi_S^{88}, \quad G_{99} = M_{99} + \Pi_S^{99} \quad (\text{A2})$$

The mass square matrix  $M$  with the daisy corrections is

$$M = \begin{pmatrix}
 M_{00} + \Pi_S^{00} & 0 & 0 & M_{03} & 0 & 0 & 0 & 0 & 0 & 0 \\
 0 & M_{11} + \Pi_S^{11} & 0 & 0 & M_{14} & 0 & 0 & 0 & 0 & 0 \\
 0 & 0 & M_{22} + \Pi_S^{22} & 0 & 0 & M_{25} & 0 & 0 & 0 & 0 \\
 M_{30} & 0 & 0 & M_{33} + \Pi_S^{33} & 0 & 0 & 0 & 0 & 0 & 0 \\
 0 & M_{41} & 0 & 0 & G_{44} & 0 & 0 & 0 & 0 & 0 \\
 0 & 0 & M_{52} & 0 & 0 & G_{55} & 0 & 0 & 0 & 0 \\
 0 & 0 & 0 & 0 & 0 & 0 & G_{66} & 0 & 0 & 0 \\
 0 & 0 & 0 & 0 & 0 & 0 & 0 & G_{77} & 0 & 0 \\
 0 & 0 & 0 & 0 & 0 & 0 & 0 & 0 & G_{88} & M_{89} \\
 0 & 0 & 0 & 0 & 0 & 0 & 0 & 0 & M_{98} & G_{99}
 \end{pmatrix} \quad (\text{A3})$$

## Appendix B: Efficiency coefficients

TABLE IV shows the relationship between efficiency coefficients for different velocities.

TABLE IV. Efficiency coefficients for different velocities.

velocities	efficiency coefficients
$v_w \ll c_s$	$\kappa_A \simeq v_w^{6/5} \frac{6.9\alpha}{1.36-0.037\sqrt{\alpha}+\alpha}$
$v_w = c_s$	$\kappa_B \simeq \frac{\alpha^{2/5}}{0.017+(0.997+\alpha)^{2/5}}$
$v_w = c_J$	$\kappa_C \simeq \frac{\sqrt{\alpha}}{0.135+\sqrt{0.98+\alpha}}$ and $c_J = \frac{\sqrt{\frac{2}{3}\alpha+\alpha^2+\sqrt{1/3}}}{1+\alpha}$
$v_w \rightarrow 1$	$\kappa_D \simeq \frac{\alpha}{0.73+0.083\sqrt{\alpha}+\alpha}$
$v_w \lesssim c_s$	$\kappa(v_w \lesssim c_s) \simeq \frac{c_s^{11/5} \kappa_A \kappa_B}{(c_s^{11/5} - v_w^{11/5}) \kappa_B + v_w c_s^{6/5} \kappa_A}$
$v_w \gtrsim c_J$	$\kappa(v_w \gtrsim c_J) \simeq \frac{(c_J-1)^3 c_J^{5/2} v_w^{-5/2} \kappa_C \kappa_D}{[(c_J-1)^3 - (v_w-1)^3] c_J^{5/2} \kappa_C + (v_w-1)^3 \kappa_D}$
$v_w = c_s$	$\delta\kappa \simeq -0.9 \log \frac{\sqrt{\alpha}}{1+\sqrt{\alpha}}$
	$\kappa(c_s < v_w < c_J) \simeq \kappa_B + (v_w - c_s) \delta\kappa + \frac{(v_w - c_s)^3}{(c_J - c_s)^3} [\kappa_C - \kappa_B - (c_J - c_s) \delta\kappa]$

### Appendix C: Fisher information

Once the probability density distribution function  $f(\Theta; x)$  is known, the logarithm of the likelihood function can be expressed as

$$l(\Theta; x) = \ln[f(\Theta; x)] \quad (\text{C1})$$

The score function is defined as the partial derivative of the natural logarithm of the likelihood function

$$\frac{\partial}{\partial \Theta} l(\Theta; x) \quad (\text{C2})$$

Fisher information (FI) represents the second cross-moment of the score vector

$$F(\Theta) = \text{E} \left[ \left( \frac{\partial}{\partial \Theta} l(\Theta; x) \right) \left( \frac{\partial}{\partial \Theta} l(\Theta; x) \right)^T \right] \quad (\text{C3})$$

Given mild regularity conditions, the score function's expected value equals zero

$$\text{E} \left[ \frac{\partial}{\partial \Theta} l(\Theta; x) \right] = 0 \quad (\text{C4})$$

As a consequence, the FI is defined as the variance of the score

$$\begin{aligned} F(\Theta) &= \text{E} \left[ \left( \frac{\partial}{\partial \Theta} l(\Theta; x) \right) \left( \frac{\partial}{\partial \Theta} l(\Theta; x) \right)^T \right] \\ &= \text{E} \left[ \left\{ \frac{\partial}{\partial \Theta} l(\Theta; x) - \text{E} \left[ \frac{\partial}{\partial \Theta} l(\Theta; x) \right] \right\} \left\{ \frac{\partial}{\partial \Theta} l(\Theta; x) - \text{E} \left[ \frac{\partial}{\partial \Theta} l(\Theta; x) \right] \right\}^T \right] \\ &= \text{Var} \left[ \frac{\partial}{\partial \Theta} l(\Theta; x) \right] \end{aligned} \quad (\text{C5})$$

TABLE V. Notation of signal analysis

variable	definition	Dimension[E]
$h_{ab}(t, \vec{x})$	metric perturbation	0
$h_A(f, \hat{k})$	Fourier coefficients of metric perturbation	-1
$S_h(f)$	strain PSD of a gravitational-wave background	-1
$\Omega_{\text{gw}}(f)$	fractional energy density spectrum of a GW background	0
$h_c(f)$	characteristic strain for GWs	0
$h_{gw}(t)$	detector response to GWs	0
$n_{gw}(t)$	detector response to noise	0
$s_{gw}(t)$	detector response	0
$\tilde{h}_{gw}(f_n)$	discrete Fourier transform of $h_{gw}(t)$	0
$\tilde{h}_{gw}(f)$	Fourier transform of $h_{gw}(t)$	-1
$\tilde{n}_{gw}(f)$	Fourier transform of $n_{gw}(t)$	-1
$S_n(f)$	strain noise PSD for a single detector	-1
$h_n(f)$	characteristic strain noise amplitude for a single detector	0

It is assumed that the observations in the sample are assumed to be independently and identically distributed. The maximum likelihood estimator, represented by  $\hat{\Theta}$ , is approximately equal to the inverse of the FI.

$$\text{Var}[\hat{\Theta}] \approx F(\Theta)^{-1} \quad (\text{C6})$$

In matrix form,  $\Theta$  is a vector with N parameters. The FI is a matrix  $F_{ij}$

$$F_{ij} = E \left[ \frac{\partial l(\Theta; x)}{\partial \Theta_i} \frac{\partial l(\Theta; x)}{\partial \Theta_j} \right] \quad (\text{C7})$$

and the inverse of FM is the covariance matrix  $C_{ij}$

$$C_{ij} = F_{ij}^{-1} \quad (\text{C8})$$

#### Appendix D: Notation and corresponding dimension of signal analysis.

TABLE V shows the notation of signal analysis and their dimension in natural units.

- 
- [1] R. D. Peccei and H. R. Quinn, Phys. Rev. Lett. **38**, 1440-1443 (1977)  
doi:10.1103/PhysRevLett.38.1440
- [2] R. D. Peccei and H. R. Quinn, Phys. Rev. D **16**, 1791-1797 (1977)  
doi:10.1103/PhysRevD.16.1791
- [3] S. Weinberg, Phys. Rev. Lett. **40**, 223-226 (1978) doi:10.1103/PhysRevLett.40.223
- [4] F. Wilczek, Phys. Rev. Lett. **40**, 279-282 (1978) doi:10.1103/PhysRevLett.40.279
- [5] J. E. Kim, Phys. Rev. Lett. **43**, 103 (1979) doi:10.1103/PhysRevLett.43.103
- [6] M. A. Shifman, A. I. Vainshtein and V. I. Zakharov, Nucl. Phys. B **166**, 493-506 (1980)  
doi:10.1016/0550-3213(80)90209-6
- [7] A. R. Zhitnitsky, Sov. J. Nucl. Phys. **31**, 260 (1980)
- [8] M. Dine, W. Fischler and M. Srednicki, Phys. Lett. B **104**, 199-202 (1981) doi:10.1016/0370-2693(81)90590-6
- [9] P. Sikivie, Rev. Mod. Phys. **93**, no.1, 015004 (2021) doi:10.1103/RevModPhys.93.015004  
[arXiv:2003.02206 [hep-ph]].
- [10] J. Preskill, M. B. Wise and F. Wilczek, Phys. Lett. B **120**, 127-132 (1983) doi:10.1016/0370-2693(83)90637-8
- [11] M. Dine and W. Fischler, Phys. Lett. B **120**, 137-141 (1983) doi:10.1016/0370-2693(83)90639-1
- [12] P. Sikivie, Lect. Notes Phys. **741**, 19-50 (2008) doi:10.1007/978-3-540-73518-2\_2 [arXiv:astro-ph/0610440 [astro-ph]].
- [13] D. Croon, R. Houtz and V. Sanz, JHEP **07**, 146 (2019) doi:10.1007/JHEP07(2019)146  
[arXiv:1904.10967 [hep-ph]].
- [14] L. Delle Rose, G. Panico, M. Redi and A. Tesi, JHEP **04**, 025 (2020)  
doi:10.1007/JHEP04(2020)025 [arXiv:1912.06139 [hep-ph]].
- [15] P. S. B. Dev, F. Ferrer, Y. Zhang and Y. Zhang, JCAP **11**, 006 (2019) doi:10.1088/1475-7516/2019/11/006 [arXiv:1905.00891 [hep-ph]].
- [16] A. Ghoshal and A. Salvio, JHEP **12**, 049 (2020) doi:10.1007/JHEP12(2020)049  
[arXiv:2007.00005 [hep-ph]].
- [17] B. Von Harling, A. Pomarol, O. Pujolàs and F. Rompineve, JHEP **04**, 195 (2020)  
doi:10.1007/JHEP04(2020)195 [arXiv:1912.07587 [hep-ph]].

- [18] C. Caprini, M. Hindmarsh, S. Huber, T. Konstandin, J. Kozaczuk, G. Nardini, J. M. No, A. Petiteau, P. Schwaller and G. Servant, *et al.* *JCAP* **04**, 001 (2016) doi:10.1088/1475-7516/2016/04/001 [arXiv:1512.06239 [astro-ph.CO]].
- [19] S. J. Huber and T. Konstandin, *JCAP* **09**, 022 (2008) doi:10.1088/1475-7516/2008/09/022 [arXiv:0806.1828 [hep-ph]].
- [20] A. Kosowsky and M. S. Turner, *Phys. Rev. D* **47**, 4372-4391 (1993) doi:10.1103/PhysRevD.47.4372 [arXiv:astro-ph/9211004 [astro-ph]].
- [21] A. Kosowsky, M. S. Turner and R. Watkins, *Phys. Rev. Lett.* **69**, 2026-2029 (1992) doi:10.1103/PhysRevLett.69.2026
- [22] M. Lewicki and V. Vaskonen, *Eur. Phys. J. C* **81**, no.5, 437 (2021) [erratum: *Eur. Phys. J. C* **81**, no.12, 1077 (2021)] doi:10.1140/epjc/s10052-021-09232-3 [arXiv:2012.07826 [astro-ph.CO]].
- [23] M. Hindmarsh, S. J. Huber, K. Rummukainen and D. J. Weir, *Phys. Rev. D* **92**, no.12, 123009 (2015) doi:10.1103/PhysRevD.92.123009 [arXiv:1504.03291 [astro-ph.CO]].
- [24] M. Hindmarsh, S. J. Huber, K. Rummukainen and D. J. Weir, *Phys. Rev. Lett.* **112**, 041301 (2014) doi:10.1103/PhysRevLett.112.041301 [arXiv:1304.2433 [hep-ph]].
- [25] C. Caprini, R. Durrer and G. Servant, *JCAP* **12**, 024 (2009) doi:10.1088/1475-7516/2009/12/024 [arXiv:0909.0622 [astro-ph.CO]].
- [26] A. Roper Pol, S. Mandal, A. Brandenburg, T. Kahniashvili and A. Kosowsky, *Phys. Rev. D* **102**, no.8, 083512 (2020) doi:10.1103/PhysRevD.102.083512 [arXiv:1903.08585 [astro-ph.CO]].
- [27] B. P. Abbott *et al.* [LIGO Scientific], *Class. Quant. Grav.* **34**, no.4, 044001 (2017) doi:10.1088/1361-6382/aa51f4 [arXiv:1607.08697 [astro-ph.IM]].
- [28] D. Reitze, R. X. Adhikari, S. Ballmer, B. Barish, L. Barsotti, G. Billingsley, D. A. Brown, Y. Chen, D. Coyne and R. Eisenstein, *et al.* *Bull. Am. Astron. Soc.* **51**, no.7, 035 (2019) [arXiv:1907.04833 [astro-ph.IM]].
- [29] E. D. Hall, *Galaxies* **10**, no.4, 90 (2022) doi:10.3390/galaxies10040090
- [30] E. D. Hall, K. Kuns, J. R. Smith, Y. Bai, C. Wipf, S. Biscans, R. X. Adhikari, K. Arai, S. Ballmer and L. Barsotti, *et al.* *Phys. Rev. D* **103**, no.12, 122004 (2021) doi:10.1103/PhysRevD.103.122004 [arXiv:2012.03608 [gr-qc]].
- [31] B. Sathyaprakash, M. Abernathy, F. Acernese, P. Ajith, B. Allen, P. Amaro-Seoane, N. Andersson, S. Aoudia, K. Arun and P. Astone, *et al.* *Class. Quant. Grav.* **29**, 124013 (2012) [erratum:

- Class. Quant. Grav. **30**, 079501 (2013) doi:10.1088/0264-9381/29/12/124013 [arXiv:1206.0331 [gr-qc]].
- [32] M. Maggiore, C. Van Den Broeck, N. Bartolo, E. Belgacem, D. Bertacca, M. A. Bizouard, M. Branchesi, S. Clesse, S. Foffa and J. García-Bellido, *et al.* JCAP **03**, 050 (2020) doi:10.1088/1475-7516/2020/03/050 [arXiv:1912.02622 [astro-ph.CO]].
- [33] R. A. Fisher, Phil. Trans. Roy. Soc. Lond. A **222**, 309-368 (1922) doi:10.1098/rsta.1922.0009
- [34] M. Pospelov and A. Ritz, Phys. Rev. Lett. **83**, 2526-2529 (1999) doi:10.1103/PhysRevLett.83.2526 [arXiv:hep-ph/9904483 [hep-ph]].
- [35] C. A. Baker, D. D. Doyle, P. Geltenbort, K. Green, M. G. D. van der Grinten, P. G. Harris, P. Iaydjiev, S. N. Ivanov, D. J. R. May and J. M. Pendlebury, *et al.* Phys. Rev. Lett. **97**, 131801 (2006) doi:10.1103/PhysRevLett.97.131801 [arXiv:hep-ex/0602020 [hep-ex]].
- [36] C. Abel, S. Afach, N. J. Ayres, C. A. Baker, G. Ban, G. Bison, K. Bodek, V. Bondar, M. Burghoff and E. Chanel, *et al.* Phys. Rev. Lett. **124**, no.8, 081803 (2020) doi:10.1103/PhysRevLett.124.081803 [arXiv:2001.11966 [hep-ex]].
- [37] Y. Asano, E. Kikutani, S. Kurokawa, T. Miyachi, M. Miyajima, Y. Nagashima, T. Shinkawa, S. Sugimoto and Y. Yoshimura, Phys. Lett. B **107**, 159 (1981) doi:10.1016/0370-2693(81)91172-2
- [38] K. Mimasu and V. Sanz, JHEP **06**, 173 (2015) doi:10.1007/JHEP06(2015)173 [arXiv:1409.4792 [hep-ph]].
- [39] J. E. Kim, Phys. Rept. **150**, 1-177 (1987) doi:10.1016/0370-1573(87)90017-2
- [40] P. Sikivie, Phys. Rev. Lett. **51**, 1415-1417 (1983) [erratum: Phys. Rev. Lett. **52**, 695 (1984)] doi:10.1103/PhysRevLett.51.1415
- [41] D. M. Lazarus, G. C. Smith, R. Cameron, A. C. Melissinos, G. Ruoso, Y. K. Semertzidis and F. A. Nezrick, Phys. Rev. Lett. **69**, 2333-2336 (1992) doi:10.1103/PhysRevLett.69.2333
- [42] S. Moriyama, M. Minowa, T. Namba, Y. Inoue, Y. Takasu and A. Yamamoto, Phys. Lett. B **434**, 147 (1998) doi:10.1016/S0370-2693(98)00766-7 [arXiv:hep-ex/9805026 [hep-ex]].
- [43] S. J. Asztalos *et al.* [ADMX], Phys. Rev. Lett. **104**, 041301 (2010) doi:10.1103/PhysRevLett.104.041301 [arXiv:0910.5914 [astro-ph.CO]].
- [44] M. S. Pshirkov and S. B. Popov, J. Exp. Theor. Phys. **108**, 384-388 (2009) doi:10.1134/S1063776109030030 [arXiv:0711.1264 [astro-ph]].

- [45] F. P. Huang, K. Kadota, T. Sekiguchi and H. Tashiro, *Phys. Rev. D* **97**, no.12, 123001 (2018) doi:10.1103/PhysRevD.97.123001 [arXiv:1803.08230 [hep-ph]].
- [46] A. Hook, Y. Kahn, B. R. Safdi and Z. Sun, *Phys. Rev. Lett.* **121**, no.24, 241102 (2018) doi:10.1103/PhysRevLett.121.241102 [arXiv:1804.03145 [hep-ph]].
- [47] C. W. Chiang and B. Q. Lu, *JCAP* **05**, 049 (2021) doi:10.1088/1475-7516/2021/05/049 [arXiv:2012.14071 [hep-ph]].
- [48] M. Ahmadvand, *JHEP* **10**, 109 (2021) doi:10.1007/JHEP10(2021)109 [arXiv:2108.00958 [hep-ph]].
- [49] J. Yang, N. Xie and F. P. Huang, [arXiv:2306.17113 [hep-ph]].
- [50] J. Yang and F. P. Huang, *Phys. Rev. D* **108**, no.10, 103002 (2023) doi:10.1103/PhysRevD.108.103002 [arXiv:2306.12375 [hep-ph]].
- [51] N. Xie and F. P. Huang, *Sci. China Phys. Mech. Astron.* **67**, no.1, 210411 (2024) doi:10.1007/s11433-023-2172-7 [arXiv:2207.11145 [hep-ph]].
- [52] P. F. Michelson, “On detecting stochastic background gravitational radiation with terrestrial detectors,” *Monthly Notices of the Royal Astronomical Society*, vol. 227, no. 4, pp. 933–941, 1987.
- [53] N. Christensen, “Measuring the stochastic gravitational-radiation background with laser-interferometric antennas,” *Physical Review D*, vol. 46, no. 12, p. 5250, 1992.
- [54] B. Allen and J. D. Romano, *Phys. Rev. D* **59**, 102001 (1999) doi:10.1103/PhysRevD.59.102001 [arXiv:gr-qc/9710117 [gr-qc]].
- [55] M. Maggiore, Oxford University Press, 2007, ISBN 978-0-19-171766-6, 978-0-19-852074-0 doi:10.1093/acprof:oso/9780198570745.001.0001
- [56] E. Thrane and J. D. Romano, *Phys. Rev. D* **88**, no.12, 124032 (2013) doi:10.1103/PhysRevD.88.124032 [arXiv:1310.5300 [astro-ph.IM]].
- [57] S. R. Coleman and E. J. Weinberg, *Phys. Rev. D* **7**, 1888-1910 (1973) doi:10.1103/PhysRevD.7.1888
- [58] L. Dolan and R. Jackiw, *Phys. Rev. D* **9**, 3320-3341 (1974) doi:10.1103/PhysRevD.9.3320
- [59] M. E. Carrington, *Phys. Rev. D* **45**, 2933-2944 (1992) doi:10.1103/PhysRevD.45.2933
- [60] P. B. Arnold and O. Espinosa, *Phys. Rev. D* **47**, 3546 (1993) [erratum: *Phys. Rev. D* **50**, 6662 (1994)] doi:10.1103/PhysRevD.47.3546 [arXiv:hep-ph/9212235 [hep-ph]].

- [61] R. R. Parwani, Phys. Rev. D **45**, 4695 (1992) [erratum: Phys. Rev. D **48**, 5965 (1993)] doi:10.1103/PhysRevD.45.4695 [arXiv:hep-ph/9204216 [hep-ph]].
- [62] P. Basler and M. Mühlleitner, Comput. Phys. Commun. **237**, 62-85 (2019) doi:10.1016/j.cpc.2018.11.006 [arXiv:1803.02846 [hep-ph]].
- [63] J. R. Espinosa, T. Konstandin, J. M. No and G. Servant, JCAP **06**, 028 (2010) doi:10.1088/1475-7516/2010/06/028 [arXiv:1004.4187 [hep-ph]].
- [64] X. Wang, C. Tian and F. P. Huang, JCAP **07**, 006 (2023) doi:10.1088/1475-7516/2023/07/006 [arXiv:2301.12328 [hep-ph]].
- [65] X. Wang, F. P. Huang and X. Zhang, [arXiv:2011.12903 [hep-ph]].
- [66] S. Jiang, F. P. Huang and X. Wang, Phys. Rev. D **107**, no.9, 095005 (2023) doi:10.1103/PhysRevD.107.095005 [arXiv:2211.13142 [hep-ph]].
- [67] A. Megevand and A. D. Sanchez, Nucl. Phys. B **825**, 151-176 (2010) doi:10.1016/j.nuclphysb.2009.09.019 [arXiv:0908.3663 [hep-ph]].
- [68] A. D. Linde, Phys. Lett. B **100**, 37-40 (1981) doi:10.1016/0370-2693(81)90281-1
- [69] A. D. Linde, “Decay of the false vacuum at finite temperature,” *Nuclear Physics B*, vol. 216, no. 2, pp. 421–445, 1983.
- [70] S. R. Coleman, Phys. Rev. D **15**, 2929-2936 (1977) [erratum: Phys. Rev. D **16**, 1248 (1977)] doi:10.1103/PhysRevD.16.1248
- [71] C. G. Callan, Jr. and S. R. Coleman, Phys. Rev. D **16**, 1762-1768 (1977) doi:10.1103/PhysRevD.16.1762
- [72] X. Wang, F. P. Huang and X. Zhang, JCAP **05**, 045 (2020) doi:10.1088/1475-7516/2020/05/045 [arXiv:2003.08892 [hep-ph]].
- [73] C. L. Wainwright, Comput. Phys. Commun. **183**, 2006-2013 (2012) doi:10.1016/j.cpc.2012.04.004 [arXiv:1109.4189 [hep-ph]].
- [74] M. Gorghetto and G. Villadoro, JHEP **03**, 033 (2019) doi:10.1007/JHEP03(2019)033 [arXiv:1812.01008 [hep-ph]].
- [75] G. Grilli di Cortona, E. Hardy, J. Pardo Vega and G. Villadoro, JHEP **01**, 034 (2016) doi:10.1007/JHEP01(2016)034 [arXiv:1511.02867 [hep-ph]].
- [76] C. O’Hare, *cajohare/AxionLimits: AxionLimits*, <https://cajohare.github.io/AxionLimits/>, [Online; accessed 16-April-2023].

- [77] S. Hamimeche and A. Lewis, Phys. Rev. D **77**, 103013 (2008) doi:10.1103/PhysRevD.77.103013 [arXiv:0801.0554 [astro-ph]].
- [78] C. Gowling and M. Hindmarsh, JCAP **10**, 039 (2021) doi:10.1088/1475-7516/2021/10/039 [arXiv:2106.05984 [astro-ph.CO]].
- [79] C. Caves, Phys. Rev. Lett. **45**, no.2, 75-79 (1980) doi:10.1103/PhysRevLett.45.75
- [80] B. P. Abbott *et al.* [LIGO Scientific and Virgo], Phys. Rev. Lett. **120**, no.9, 091101 (2018) doi:10.1103/PhysRevLett.120.091101 [arXiv:1710.05837 [gr-qc]].
- [81] P. A. Rosado, Phys. Rev. D **84**, 084004 (2011) doi:10.1103/PhysRevD.84.084004 [arXiv:1106.5795 [gr-qc]].
- [82] S. Sachdev, T. Regimbau and B. S. Sathyaprakash, Phys. Rev. D **102**, no.2, 024051 (2020) doi:10.1103/PhysRevD.102.024051 [arXiv:2002.05365 [gr-qc]].